Austenite formation from a steel microstructure containing martensite/austenite and bainite bands

Abraham Mathews, J.; Sietsma, J.; Petrov, R. H.; Santofimia, M. J.

DOI
10.1016/j.jmrt.2023.06.270

Publication date
2023

Document Version
Final published version

Published in
Journal of Materials Research and Technology

Available online at www.sciencedirect.com

jmr&t Journal of Materials Research and Technology

journal homepage: www.elsevier.com/locate/jmrt

Austenite formation from a steel microstructure containing martensite/austenite and bainite bands

J. Abraham Mathews [a,*], J. Sietsma [a], R.H. Petrov [a,b], M.J. Santofimia [a]

[a] Department Materials Science and Engineering, Delft University of Technology, Mekelweg 2, 2628 CD, Delft, the Netherlands

[b] Department of Electrical Energy, Metals, Mechanical Constructions & Systems, Ghent University, Technologiepark 46, 9052 Ghent, Belgium

ARTICLE INFO

Article history:
Received 5 May 2023
Accepted 29 June 2023
Available online 6 July 2023

Keywords:
Austenite formation
Bimodal grain size
Carbide-dense bands
In situ XRD

ABSTRACT

In many commercial steel processing routes, steel microstructures are reverted to an austenitic condition prior to the final processing steps. Understanding the microstructure development during austenitization is crucial for improving the performance and reliability of the microstructure that forms from austenite. In this work, austenite formation in a high-C steel (0.85 wt%) from a microstructure containing martensite/austenite and bainite bands is investigated. It is shown that austenite formation from bainite results in a refined austenite grain structure, and the martensite matrix thus obtained on quenching has a homogeneous distribution of carbides with a relatively low fraction of retained austenite (24%). On the other hand, a coarser austenite microstructure is obtained when austenite forms from a mixture of martensite and retained austenite. The reason for the coarse austenite grains is argued to be a memory effect, which is substantiated by in situ X-ray diffraction analysis. After quenching, an inhomogeneous carbide distribution and a higher retained austenite fraction (30%) are observed in the regions that were initially martensite/austenite. The global microstructure, hence, has a bimodal size distribution of prior austenite grains and carbide-dense bands. The causes for these heterogeneities are discussed with the help of interrupted quench experiments, equilibrium phase calculations, and DICTRA simulations.

1. Introduction

Many steel components used in industrial applications undergo a heat treatment that reverses their microstructure to austenite for the purpose of grain refinement [1–3]. This heat treatment is called hardening, and typically involves isothermal holding at an austenite formation temperature, followed by quenching to obtain martensite. The formation of martensite is confined within each parent austenite grain and results in a high density of lath, block, and packet boundaries [4,5]. These sub-structures act as barriers to dislocation motion, which increases the strength of martensite [6]. The density of these sub-structures is well-known to be affected by the prior-austenite grain size [5,6]. A hardened microstructure of fine-grained martensite has several advantages over coarse-grained martensite in terms of mechanical properties, such as tensile strength [7,8], fatigue strength [9,10],

* Corresponding author.
E-mail address: j.abrahammathews@tudelft.nl (J. Abraham Mathews).
https://doi.org/10.1016/j.jmrt.2023.06.270

and toughness [11,12], which is the motivation for creating a fine austenite microstructure.

Therefore, the properties of martensite are governed by the microstructural changes occurring during austenite formation; partitioning of carbon and other alloying elements, carbide precipitation, dissolution of secondary phases, austenite grain size development, etc. These changes accompanying austenite formation have been reported in the literature to depend on the heating rate [13–15], initial microstructure [15,16], and the holding time and temperature. In conventional hardening treatments, the heating rates are such that the initial microstructure and its decomposition products formed during continuous heating are eventually austenitic at the hardening temperature due to the rapid kinetics of austenite formation. However, solubility and diffusivity differences for the alloying elements in different microstructural constituents engender different durations for these elements to homogeneously distribute in austenite. Consequently, the compositional homogeneity of the austenite matrix can be to different degrees, which makes austenite formation during hardening sensitive to the initial microstructure.

One of the most widely studied initial microstructures for austenite formation is ferrite-pearlite [15,17–20]. A general conclusion in these studies is that austenite formation occurs in two stages: rapid growth of austenite into pearlite, and subsequent slow transformation of ferrite into austenite. During the reversion of the ferrite-pearlite microstructure, transformation begins with the nucleation of austenite at ferrite/pearlite interfaces, where grains grow relatively rapidly into the adjacent pearlite due to the short required diffusion distances for carbon [15,19]. A high density of ferrite/pearlite interfaces results in a correspondingly high density of favorable sites for austenite nucleation. Consequently, the density of austenite grains per unit volume is also high, resulting in a fine structure [21].

While austenite grows with an equiaxed morphology from a ferrite-pearlite microstructure [22], two types of morphologies are reported when austenite forms from bainitic or martensitic microstructures: “globular” and “acicular” [22–26]. Globular austenite grains form at the prior austenite grain boundaries while the acicular austenite grains form at bainite or martensite lath boundaries [25]. In certain cases, recovery of the shape, size, and orientation of the prior austenite grains occurs when a bainitic or martensitic microstructure is reheated into the austenitic region. This phenomenon is called the “austenite memory effect” and transpires by the growth of acicular austenite [23,26,27]. At least three different mechanisms for the memory effect are proposed in the literature: diffusionless shear mechanism [28], growth and coalescence of retained austenite [23,27], and variant restriction between reversed austenite, cementite, and martensitic laths [29]. A common aspect in these studies is that the nucleation and growth of the more dominant form of nuclei (globular or acicular) depend on the heating rate and the initial presence of retained austenite.

In addition to the austenite grain size, the composition of the austenite matrix developed during the hardening treatment is vital in determining the properties of martensite. It is a general practice in the hardening treatment to eliminate ferrite and carbides in medium-C steels, but cementite often remains undissolved in high-C steels. Fine and uniform distribution of cementite in the hardened microstructure is beneficial for applications that demand high wear resistance [30]. However, an inhomogeneous distribution of carbides in the form of bands is detrimental as it drastically reduces fatigue and wear resistance [31]. There is only very sparse literature on carbide banding in high-carbon steels [32–36], which is of specific interest in this study. Despite the limited literature, there is a general agreement that the reason for carbide-band formation is related to chemical inhomogeneities stemming from solidification segregation.

Austenite formation is reported in the literature mostly for low-carbon steels with elements that either stabilize austenite (Ni/Mn) or tend to form carbides (Cr). However, certain steels used in demanding load-bearing applications require a combination of strength, toughness, and wear resistance. A combination of these properties requires high-alloy steels, often containing high Ni and Cr concentrations, to produce a martensitic matrix (for strength) with a homogeneous distribution of retained austenite (for toughness) and carbides (for wear resistance). Annealing treatments, prior to hardening, on these high-alloy steels have been shown to produce microstructures containing martensite/austenite and bainite bands [37]. Austenite formation from such banded microstructures is poorly understood. The present work investigates the hardening treatment from an initial microstructure consisting of bainite and martensite/austenite bands in Ni, Cr-containing high-C steel. The hardened microstructure is observed to have a bimodal austenite grain size distribution, carbide-dense bands, and heterogeneous distribution of retained austenite. The rationale behind the experimental observations is elucidated by studying the microstructure development during the heat treatment with the help of in situ X-ray diffraction experiments, interrupted-quench experiments, equilibrium phase calculations, and diffusion simulations.

2. Material and experimental methods

The investigated material is a high-carbon steel containing Ni and Cr, with the specific composition as shown in Table 1.

2.1. *Initial microstructure*

The initial microstructure used in this study is the same as in a previous study by the present authors [37] and is shown in

Table 1 – Composition of the investigated steel.

Elements	C	Ni	Cr	Mo	Si	Mn	P	S	Fe
Wt.%	0.85	3.3	1.5	0.2	0.4	0.55	0.007	0.003	Bal.

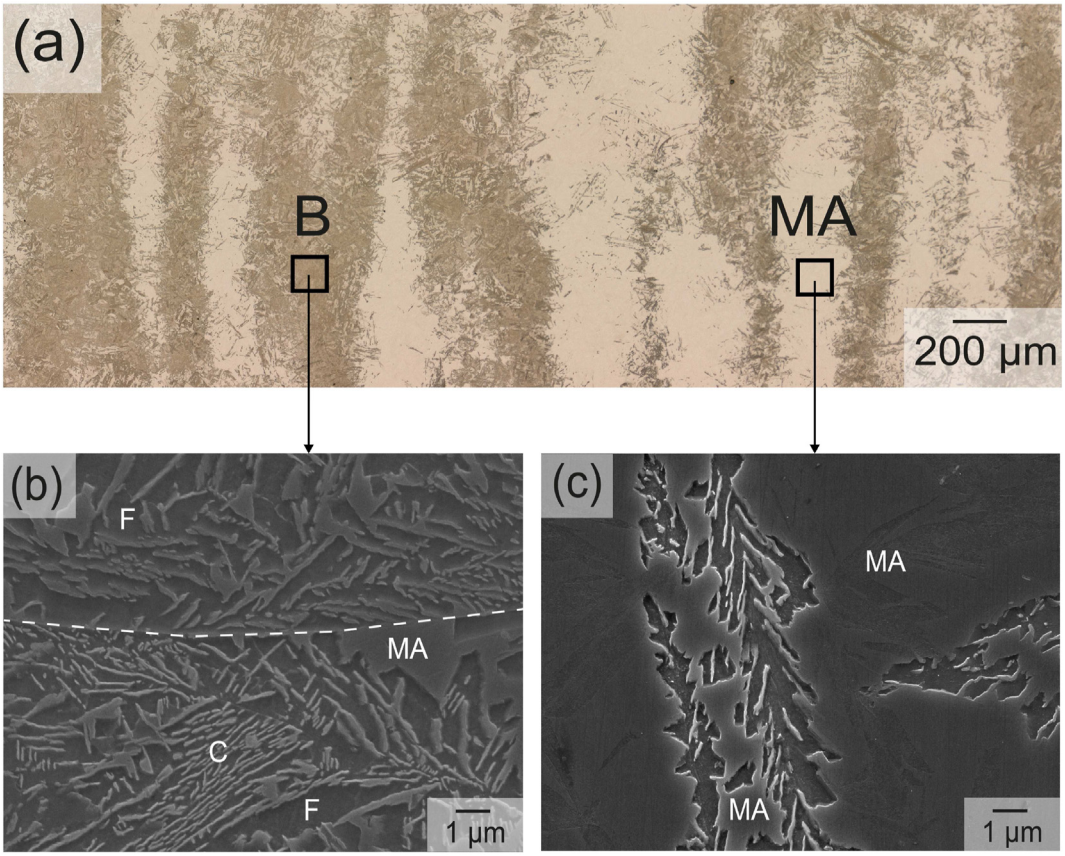

Fig. 1 – Initial microstructure used in this study, obtained after 30 h of isothermal treatment at 320 °C, followed by quenching to room temperature. (a) Optical micrograph showing bainite (dark) and martensite/austenite (light) bands. (b) and (c) are SEM micrographs from the bainite and martensite/austenite regions, respectively. The white dashed line in (b) indicates a prior austenite grain boundary. B: bainite, F: bainitic ferrite, MA: martensite/austenite, and C: cementite.

Fig. 1. The steel has chemical segregation bands, with solute-lean and solute-rich regions of Ni, Cr, Mn, Mo, and Si. Due to chemical segregation, the applied heat treatment (refer to Ref. [37]) resulted in a banded microstructure consisting of bainite bands and martensite/austenite bands, as shown in Fig. 1(a). The volume fraction of the phases present in this microstructure were quantified using XRD analysis. The results show 43 ± 2 vol% BCC (bainitic ferrite), 31 ± 4 vol% FCC (austenite), 23 ± 5 vol% BCT (martensite), and 3 ± 1 vol% cementite. The fractions of bainitic ferrite and cementite belong to the solute-lean region, while the fractions of martensite and austenite belong to the solute-rich region. It should be noted that the tetragonal martensite (BCT) peaks were clearly distinguishable from the ferrite (BCC) peaks, allowing for accurate quantification of the martensite fraction. This distinctive nature of the martensite peaks has been previously established and documented in our earlier work [37]. Scanning Electron Microscopy (SEM) micrographs from the solute-lean (bainite) and solute-rich (martensite/austenite) regions are shown in Fig. 1(b) and (c), respectively.

2.2. *Experimental procedure*

Heat treatments were performed in a Bähr 805A quench dilatometer on specimens of dimensions 10 × 3 × 1 mm^3 (x × y × z). For the hardening treatment, the specimen was heated to 840 °C at a heating rate of 0.5 °C/s and isothermally held for 7200 s. After the isothermal holding period, the specimen was cooled in He at a cooling rate of 50 °C/s. To understand the microstructure evolution at the hardening temperature (840 °C), interrupted-quench experiments were made at 10, 300, and 3600 s using the same heat treatment parameters as employed for the hardening treatment. A schematic of the applied heat treatments is shown in Fig. 2.

The metallographically prepared specimens were etched in 5% Nital solution for microstructural investigations using optical and scanning electron microscopes (SEM). Optical micrographs were captured using a Keyence VHX-6000 microscope. SEM micrographs were taken using a JEOL JSM-6500 F field emission gun scanning electron microscope operated at an accelerating voltage of 15 kV.

Electron Back Scatter Diffraction (EBSD) experiments were made on an FEI Quanta 450 scanning electron microscope. The EBSD patterns were acquired using OIM data collection software under the following operational parameters: acceleration voltage of 20 kV, specimen tilt angle of 70°, and a step size of 50 nm on a hexagonal scan grid. TSL OIM Analysis 7.0 was used for the post-processing of the EBSD data.

Elemental segregation (Ni, Cr, Mn, Si, and Mo) was quantified using a JEOL JXA 8900 R microprobe employing

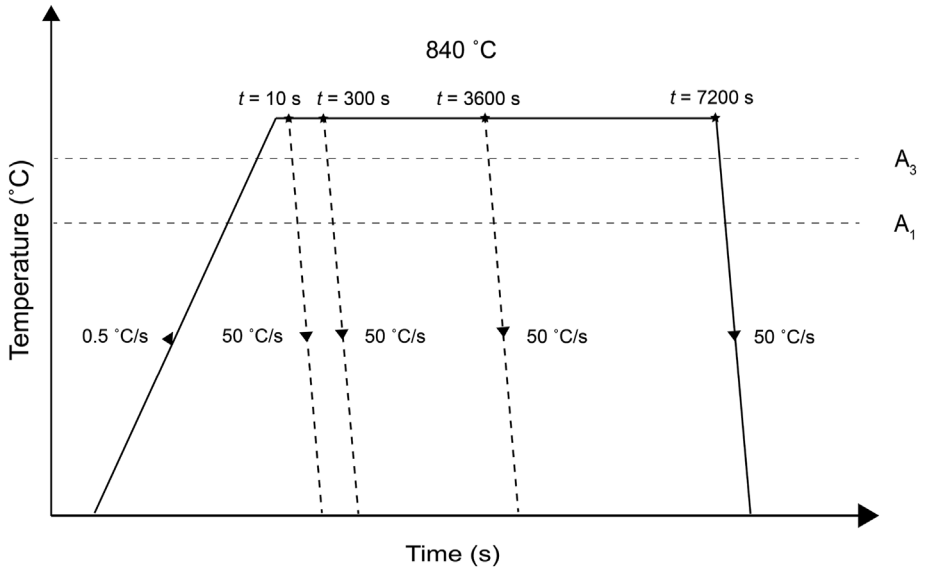

Fig. 2 – Schematic representation of the applied heat treatments.

wavelength dispersive spectroscopy. The measurements were made with a step size of 2 μm along a line of ≈ 600 μm at an electron beam energy of 15 keV and a beam current of 50 nA.

The volume fractions of the phases were determined using X-ray diffraction (XRD) experiments. A Bruker D8-Advance diffractometer with CoKα-radiation was used to scan a 2θ range of 40° to 130°. The counting time per step was 4 s with a step size of 0.035° 2θ. The volume fractions of austenite (FCC) and martensite (BCC) were calculated from the net integral intensities of five FCC peaks ({111}, {200}, {220}, {311}, and {222}) and four BCC peaks ({110}, {200}, {211}, and {220}). The evaluation of data was made using Bruker's DiffracSuite EVA software (version 6.0), Profex/BGMN, employing Rietveld refinement for the quantification of the detected phases. The error in the volume fractions of the phases measured by XRD analysis is ± 1 vol%.

In situ XRD experiments were performed on a Bruker D8 diffractometer equipped with a Vantec-500 2D area detector. A specimen of dimensions 20 × 4 × 1 mm^3 (x × y × z) was clamped to an Anton Paar DHS1100 heating stage, and heated to 850 °C at a heating rate of 0.5 °C/s. The hardening temperature in the in situ XRD experiment was calibrated prior to the experiment. A graphite dome was used during the experiment, into which He gas was circulated to avoid oxidation of the specimen during the heat treatment. The side of the specimen having a carbon concentration of 0.85 wt% was irradiated with CoKα-radiation and diffraction patterns were acquired every 30 s using a beam with a spot diameter of 1 mm. The XRD patterns were recorded in the range of 48° to 105° 2θ in reflection mode. The scans comprise three austenite (γ) peaks: {111}γ, {200}γ, and {220}γ.

The hardness measurements were made on a Dura-scan 70 (Struers) hardness tester using a Vickers indenter. A load of 9.8 N was applied for a dwell time of 10 s, and at least 10 measurements were used in the calculation of the average hardness values.

2.3. *DICTRA simulations*

The dissolution behavior of cementite and the redistribution of alloying elements during 2 h of isothermal holding at the austenitization temperature (840 °C) is studied by performing DICTRA simulations using the TCFE11 and MOBFE7 databases. The simulation domain is defined as a one-dimensional (1D) space, in which the widths of the austenite and cementite phases were defined as 3750 nm and 150 nm, respectively, with a planar interface. The 1D simulation system was chosen to represent the 3D microstructure in spherical geometry for the defined phases.

Mo, Si, P, and S were excluded from the simulation for numerical stability reasons. Austenite and cementite are assumed to have a homogeneous composition profile for Ni, Mn, and Cr. The values assumed in the simulation are the same as shown in Table 1. The carbon composition in austenite was set to 0.8 wt%, which is the equilibrium value for the chosen simulation composition at 840 °C. The DICTRA simulations were performed under closed boundary conditions in which the concentration of the diffusing species is maintained constant.

3. Results

The microstructure obtained after the hardening treatment (2 h at 840 °C) is shown in Fig. 3(a). This optical micrograph shows a martensite matrix with dark etching regions (DER) and light etching regions (LER). The contrast between the two regions arises from microstructural inhomogeneities, which are discussed in sections 3.1 and 3.2. The average hardness of the dark etching regions is 773 ± 2 HV, which is ≈ 50 HV more than the average hardness of the light etching regions (721 ± 2 HV). The volume fractions of the

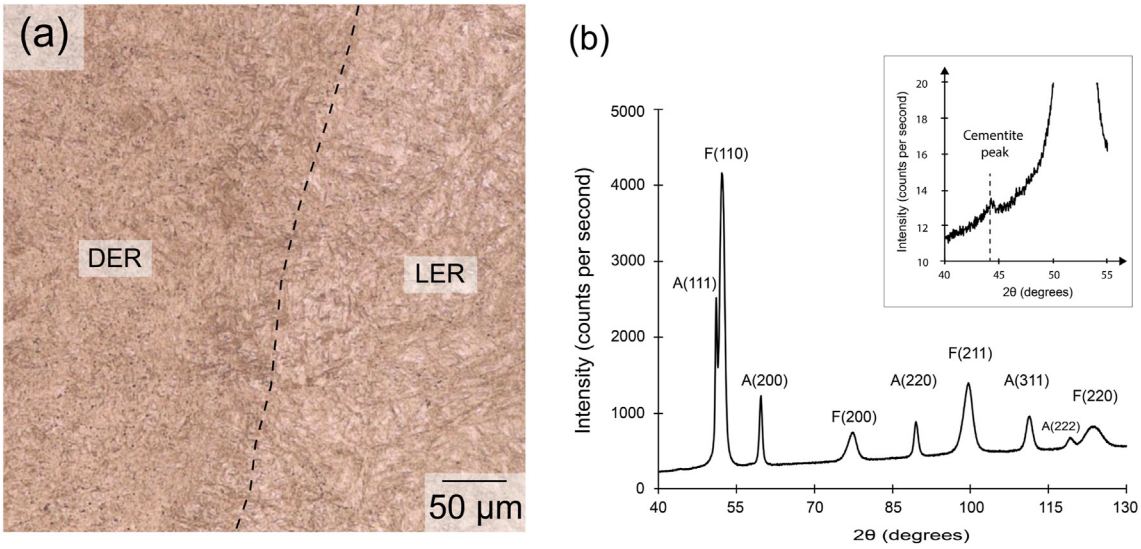

Fig. 3 – (a) Optical micrograph of the hardened microstructure showing the dark and light etching regions, DER and LER, respectively. The dotted line shows an indication of the boundary between these two regions. (b) X-ray diffractogram with the identified phases, where A = austenite and F = ferrite. The inset in this figure shows an example of a cementite peak.

phases quantified from the overall microstructure using XRD analysis are 71 ± 1 vol% BCC, 26 ± 1 vol% FCC, and 3 ± 1 vol% cementite (θ). The diffraction patterns with the identified phases are shown in Fig. 3(b). Note that the weaker intensity of the cementite peaks compared to BCC and FCC results in concealing these peaks on this scale, which, however, are present and can be quantified. An example of the cementite peak is shown in the inset of Fig. 3(b).

The distribution of DER and LER is associated with the chemical bands present in the starting microstructure, which is investigated by quantifying the segregation profiles of Ni, Cr, Mn, Si, and Mo by EPMA measurements. The results are shown in Fig. 4. The optical micrograph in this figure shows the region across which the measurements were made. The average of 301 measurements for each element is taken as its nominal composition, represented by dotted lines. The concentrations of Cr, Mn, Si, and Mo are plotted on the primary vertical axis and that of Ni on the secondary vertical axis. Fig. 4 shows that the concentrations of Ni, Cr, Mn, and Si lie predominantly below their nominal concentration in the DER and predominantly above their nominal concentration in the LER. Therefore, dark etching regions (DER) are solute-lean, and light etching regions (LER) are solute-rich. The profile for Mo is seen to have a high degree of scattering across its nominal value in both regions. From the analyses, it is interpreted that the microstructure in the DER is a result of austenite formation from regions that were previously bainite while LER results from the austenite formation from regions that were previously a mixture of martensite and retained austenite [37].

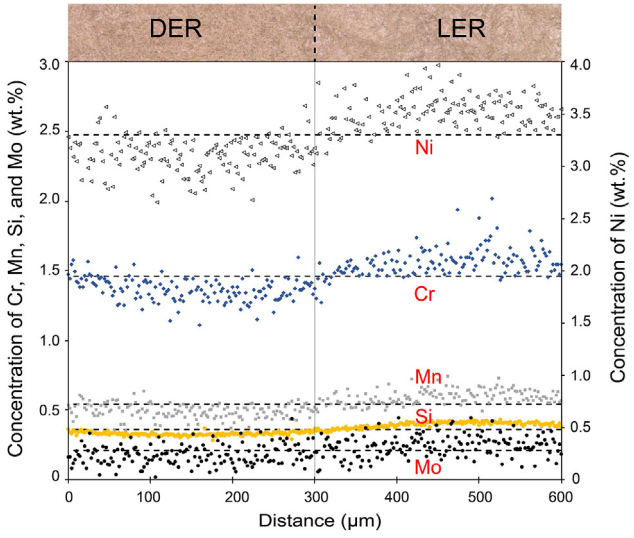

Fig. 4 – Concentration profiles of Ni, Cr, Mn, Si, and Mo in the hardened microstructure measured using EPMA.

3.1. *Microstructure characterization of the solute-lean region (DER)*

The SEM micrograph from the solute-lean region (DER) is shown in Fig. 5(a). The microstructural constituents in this region are martensite, martensite-austenite (MA) islands, and cementite. The martensite matrix has a lower surface relief since it is etched deeper than the MA islands. A homogeneous distribution of cementite that has mostly a globular morphology is observed in the DER. The distribution and the morphology of cementite are more noticeable from the contrasted SEM micrograph shown in Fig. 5(b). The area fraction of cementite is quantified as 3% using image analysis with ImageJ software. The spatial distribution of these phases in the hardened microstructure is studied by EBSD analysis. The phase map (PM) superimposed on the image quality (IQ) map from DER is shown in Fig. 5(c). Red and green regions in the phase map correspond to BCC (martensite) and FCC (austenite) crystal structures, respectively. Non-indexed

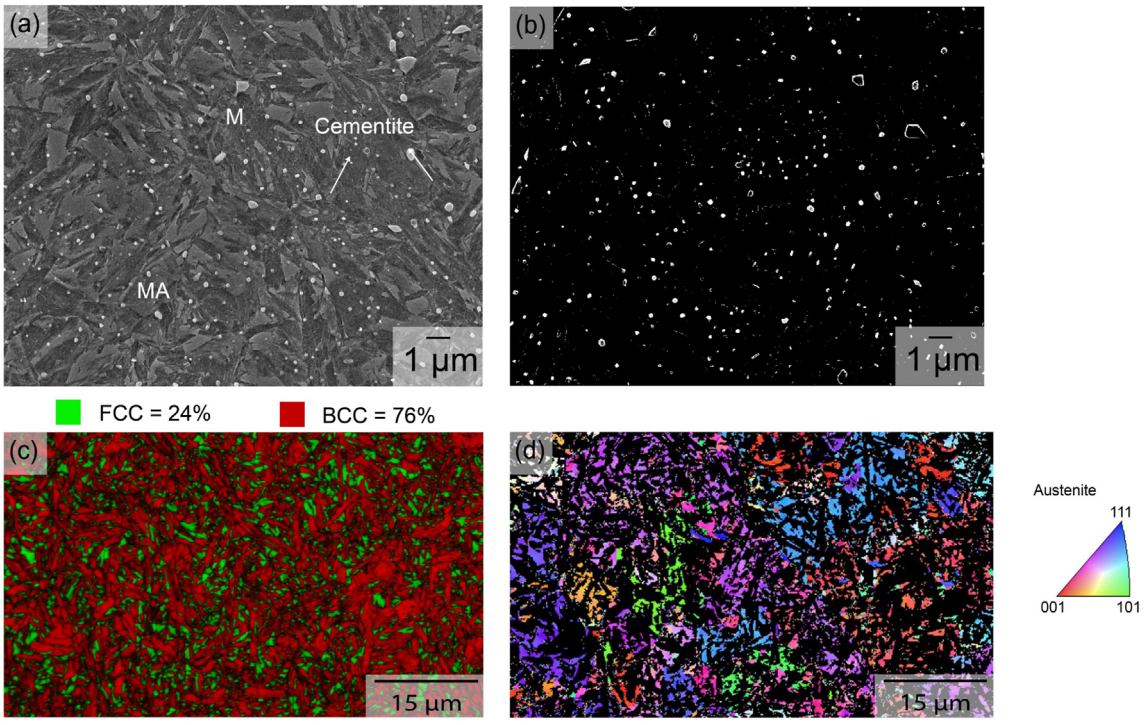

Fig. 5 – Characterization results of the hardened microstructure from the solute-lean region (DER): (a) SEM micrograph, (b) contrasted image from the region shown in (a), (c) phase map combined with image quality map, (d) inverse pole figure map of austenite. M: martensite and MA: martensite/austenite.

points in this map are black. To reduce the possibility of mis-indexation of phases, the diffraction patterns of cementite were excluded from the measurement. This is because cementite can produce weak and diffuse diffraction patterns, which can lead to difficulties in accurately distinguishing and indexing individual phases. Phase quantification from EBSD shows 24% austenite in the DER. The inverse pole figure (IPF) map of austenite from DER is shown in Fig. 5(d). Each color in this map corresponds to a specific crystal orientation of austenite. A cluster of austenite grains with the same color (same crystal orientation) represents a prior austenite grain. Several clusters of austenite grains of the same orientation constituting a prior austenite grain can be seen in the DER.

3.2. *Microstructure characterization of the solute-rich region (LER)*

The SEM micrograph from the solute-rich region (LER) is shown in Fig. 6(a). The microstructural constituents in this region are the same as in the solute-lean region (DER); martensite, martensite-austenite (MA) islands, and cementite. The main difference between the two regions is the distribution and morphology of cementite. Unlike the solute-lean region, where a homogeneous distribution of cementite is observed (see Fig. 5(a and b)), cementite distribution is inhomogeneous in the solute-rich region. In addition to the globular morphology, the elongated plate-like morphology of cementite is observed to be grown along the martensite laths in the LER. The distribution and the morphology of cementite in this region are shown in the contrasted SEM micrograph, Fig. 6(b). The spatial distribution of the phases in the solute-rich region of the hardened microstructure is shown in Fig. 6(c). The explanation of the microstructural constituents representing each color in this IQ + phase map is the same as discussed in section 3.1. Local phase quantification from the phase maps shows that there is a considerably higher fraction of austenite in the solute-rich region (LER): 30%, compared to 24% in the solute-lean region (DER). The inverse pole figure (IPF) map of austenite from this region is shown in Fig. 6(d). Unlike the orientation spread observed for the austenite grains in the solute-lean region (see Fig. 5(d)), the scanned area of the solute-rich region shows primarily only two prior austenite grains. A comparison of Figs. 5(d) and Fig. 6(d) reveals that the prior austenite grains are coarser in the solute-rich regions (LER) in comparison to the solute-lean regions (DER).

3.3. *Summary of the hardened microstructure*

The hardened microstructure exhibits microstructural variations. Solute-lean regions (previously bainite) of the hardened microstructure display finer prior austenite grains, whereas those in the solute-rich regions (previously martensite/austenite) are coarser. The distribution of carbides and retained austenite are also different (see Figs. 5 and 6). The solute-lean regions have a homogeneous distribution of cementite, which has a globular morphology (see Fig. 5(a and b)). On the other hand, the solute-rich regions have an inhomogeneous distribution of fine globular carbides and carbides of elongated rod-like morphology. Additionally, these regions

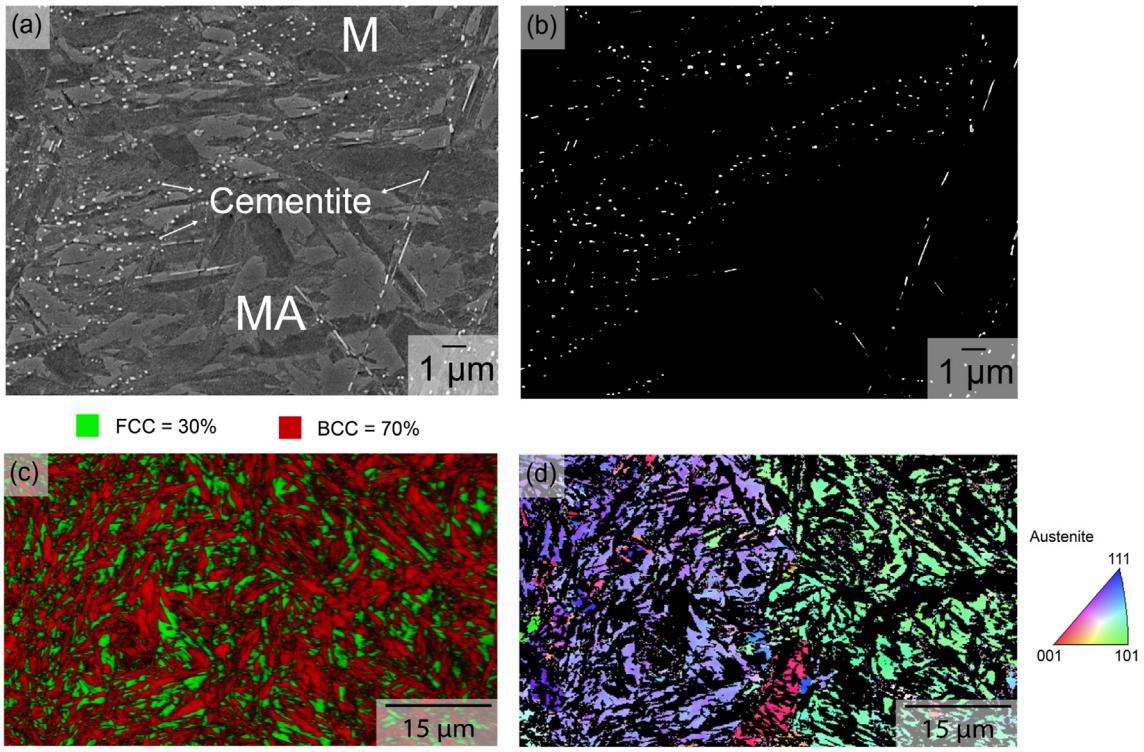

Fig. 6 – Characterization results of the hardened microstructure from the solute-rich region (LER): (a) SEM micrograph, (b) contrasted image from the region shown in (a), (c) phase map combined with image quality map, (d) inverse pole figure map of austenite. M: martensite and MA: martensite/austenite.

have a higher fraction of retained austenite compared to solute-lean areas. The overall microstructure, therefore, has "carbide-dense bands" as a result of the variations in the distribution, size, and density of the carbide particles. A summary of these differences is shown in Table 2.

4. Discussion

The hardened microstructure is heterogeneous in terms of (i) prior austenite grain size, (ii) phase distribution, and (iii) carbide morphology and its spatial distribution. A schematic of the differences listed in Table 2 is shown in Fig. 7. To obtain further insight into the differences in austenite grain size and phase heterogeneities, microstructural evolution during the hardening treatment is studied using in situ XRD and interrupted quench experiments.

4.1. *Prior austenite grain size variations in the hardened microstructure*

The initial microstructure in the solute-lean regions is bainitic, while solute-rich areas are a mixture of martensite and retained austenite (see Fig. 1). The microstructural changes associated with austenite can be studied by following the change in its fraction during continuous heating. Trailing the austenite fraction during heating is critical as the austenite formation mechanism may change from nucleation-aided to the one transpiring by the growth of existing austenite [27], if austenite persists as a metastable phase until A_{c1}. The change in the retained austenite fraction during heating to the hardening temperature **(840 °C)**, determined by in situ XRD, is shown in Fig. 8.

Retained austenite is observed to be stable up to 320 °C from the in situ XRD analyses shown in Fig. 8. Beyond this temperature, austenite decomposes such that its initial

Table 2 – Summary of the microstructural differences in the solute-lean and solute-rich regions after hardening.

	Solute-lean region (DER)	Solute-rich region (LER)
Prior microstructure	bainite	martensite and retained austenite
Cementite distribution	homogeneous	inhomogeneous
& morphology	globular	globular, elongated plate-like
Retained austenite fraction	24%	30%
Hardness	773 ± 2 HV	721 ± 2 HV
Prior austenite grains	fine	coarse

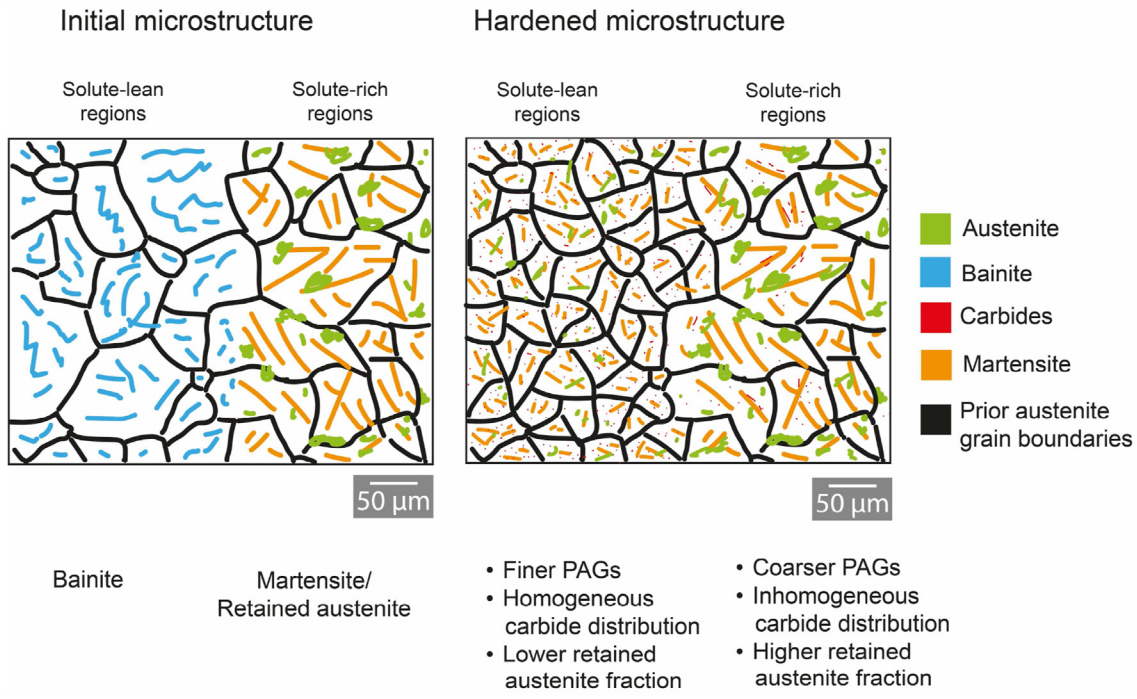

Fig. 7 – Schematics of the initial and hardened microstructures.

volume fraction of 25 ± 4 vol% decreases to 20 ± 4 vol% at 420 °C. The decomposition products of austenite during heating are generally proposed to be a mixture of ferrite and cementite [22]. The fraction of austenite in the temperature range between 420 °C and 620 °C does not vary significantly, implying no further decomposition of austenite beyond 420 °C. The plateau in the austenite fraction indicates local variations in the carbon concentrations of retained austenite present in the starting microstructure. Austenite with higher carbon concentrations possesses higher thermal stability. Consequently, islands of the austenitic phase that are more enriched in carbon remain metastable during heating. When the temperature exceeds the austenite-start temperature, A_{c1} (636 °C), the volume fraction of austenite increases rapidly and the

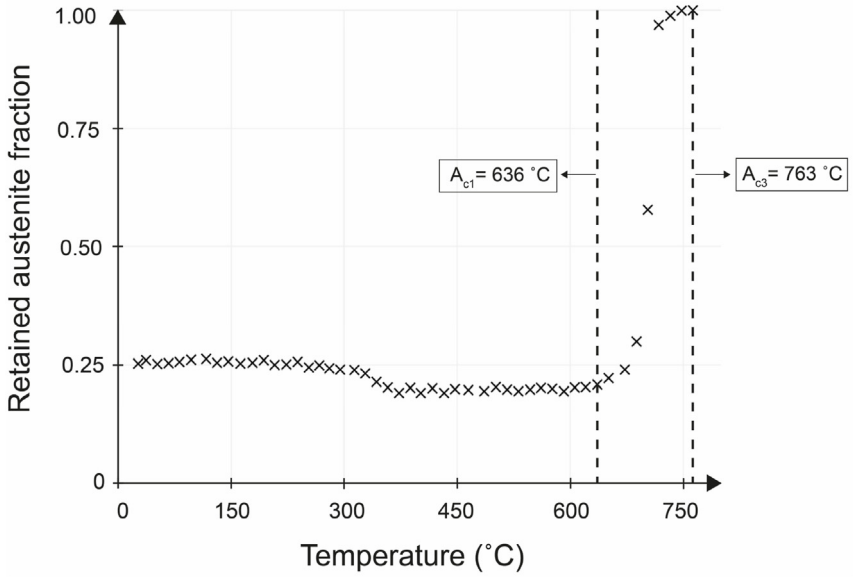

Fig. 8 – Change in the fraction of retained austenite (present in the initial microstructure) with temperature during continuous heating, determined by in situ XRD.

austenite fraction reaches 100% at 763 °C, which is the A_{c3} temperature.

In situ XRD analysis reveals that continuous heating to the hardening temperature does not eliminate the initially present austenite in the solute-rich regions. Therefore, the austenite retained in these regions can grow when the temperature is above A_{c1} without the need for nucleation. On the other hand, austenite formation in the solute-lean regions, devoid of retained austenite, occurs inevitably through the nucleation and growth of new austenite grains. Numerous studies have shown that austenite formation from microstructures containing retained austenite can occur without nucleation and in some cases reconstitutes the prior austenitic grains, with respect to crystallography, size, and shape [23,27,28,38,39]. This phenomenon is called the austenite memory effect. Such a "memory effect" restrains grain refinement [22]. Therefore, it is necessary to evaluate the occurrence of the austenite memory effect in the investigated steel. This evaluation is performed by comparing the prior austenite grain sizes of the initial (Fig. 1(a)) and the hardened (Fig. 3(a)) microstructures.

The prior austenite grains of the initial microstructure (Fig. 1(a)) were formed during the preceding carburization treatment. As bainite and martensite formations are confined within an austenite grain, etchants that reveal the prior austenite grain boundaries can be used for grain size quantification [40]. However, cementite present in this microstructure reacts to the etchant in a way that obscures the prior austenite grain boundaries, and prevents good etching results. Therefore, a specimen of the same carbon content (0.85 wt%) that is directly quenched after carburization is availed for the prior austenite grain size quantification of the initial microstructure. The optical micrograph of the prior austenite grain boundaries and a chart of the grain size distribution of the corresponding microstructure are shown in Fig. 9. Grain size quantification was made using the linear intercept method by counting 385 grains. Note that this optical micrograph includes the solute-lean and solute-rich regions as the width of this micrograph is more than three times the width of the chemical segregation bands, which is less than 300 μm (see Fig. 4). The chart in Fig. 9 shows that ≈ 32% of the grains fall within the size range of 40–60 μm. The grain size distribution has an average value of 80 μm with a 95% confidence interval of 75.98 μm–84.02 μm, based on a sample size of 385 grains. The standard deviation of the grain size distribution is 40 μm. A bimodal distribution of prior austenite grains is not observed. As the austenite grain size distribution shown in Fig. 9 is representative of the initial microstructure (Fig. 1), it is inferred that there is no bimodal distribution of austenite grains in the initial microstructure.

The prior austenite grains of the hardened microstructure are evaluated by reconstructing the parent austenite grains from the EBSD data of Figs. 5(c) and 6(c). The reconstructed austenite grains from the solute-lean (DER) and solute-rich (LER) regions are shown in Fig. 10(a) and (b), respectively. The reconstruction is based on the Nishiyama-Wasserman orientation relationship between the austenite (parent) and martensite (child) grains. Each color in Fig. 10 represents a specific orientation of austenite. It is evident from this figure that the density of austenite grains in the solute-lean regions is considerably higher than in the solute-rich regions. The prior austenite grain size in the solute-lean regions is in the range 5–20 μm, while it is at least more than 40 μm in the solute-rich regions based on the measured area as seen in Fig. 10(b). These results indicate a bimodal distribution of prior austenite grains for the hardened microstructure.

The austenite grain size of the hardened microstructure in the solute-lean region (DER) is smaller by a factor of approximately four than in the initial microstructure. This shows that austenite formation from bainite (solute-lean regions) results in grain refinement. The initial bainite microstructure in the solute-lean region has a dense distribution of thin plates of cementite. The numerous cementite/ferrite interfaces in bainite are typical austenite nucleation sites [41,42] as the cementite provides a high concentration of carbon, which is necessary for the formation of austenite. Therefore, the

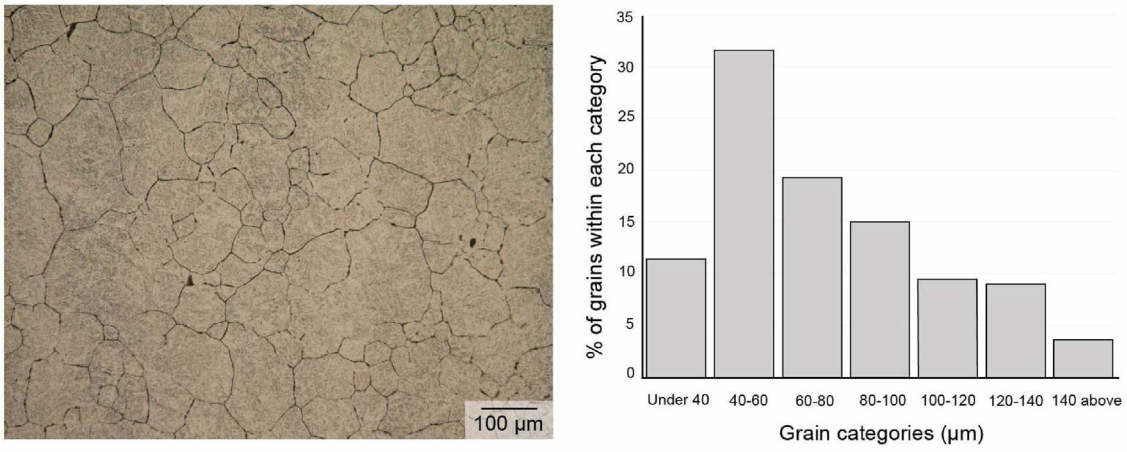

Fig. 9 – Optical micrograph showing the prior austenite grain boundaries of the specimen containing 0.85 wt %C, heat treated for 60 h at 970 °C. Note that the prior austenite grain size characteristics observed in this figure are representative for the initial microstructure used in the current study due to the same austenitization conditions.

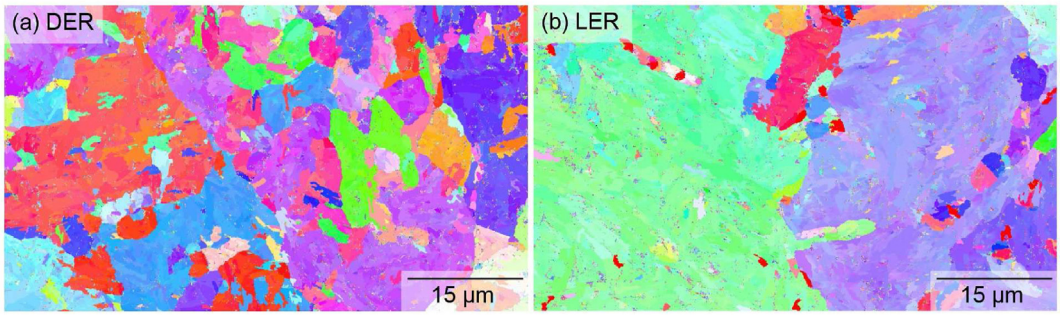

Fig. 10 – Reconstructed EBSD images of the prior austenite grain boundaries in the (a) solute-lean region (DER) and (b) solute-rich region (LER) of the hardened microstructure.

nucleation density of austenite is high, which results in a fine grain structure.

However, the austenite grain sizes before and after the hardening treatment are similar when austenite formation is from a martensitic structure containing retained austenite (solute-rich regions). This similarity indicates the inhibition of grain refinement. Despite the lack of direct evidence to associate the inhibition of grain refinement due to the austenite memory effect, available experimental results allude to their interdependence: (i) a significant fraction of austenite is retained during continuous heating, and (ii) similarities in the austenite grain sizes before and after the hardening treatment. Conjoining these observations, it is presumed that the inhibition of grain refinement in the solute-rich regions is due to the growth and coalescence of the existing austenite, which reconstitutes the coarse prior austenitic grain structure. Such a growth process is kinetically and energetically more favorable than the nucleation of new grains as the latter phenomenon requires the creation of new interfaces which consumes more energy.

4.2. *Heterogeneous phase distribution in the hardened microstructure*

The hardening temperature (840 °C) falls within the austenite-cementite phase field for the investigated steel according to ThermoCalc calculations (TCFE11 database). Due to the high carbon content, the martensite-start temperature is low with respect to room temperature. Therefore, the hardened microstructure should contain not only martensite and cementite but also retained austenite. However, the uneven distribution of these phases in the microstructure requires further investigation.

The heat treatment response of the solute-rich and solute-lean regions is different during the hardening treatment due to the different starting microstructures. Consequently, it is possible for these regions to transform into different products at different times during the heat treatment. Composition-induced microstructural heterogeneities are widely reported in literature [32,43–45]. To investigate this phenomenon, the equilibrium fraction of phases at 840 °C was calculated for the average chemical composition of each of the two regions. The average chemical composition is quantified from the EPMA results (Fig. 4), assuming a constant carbon content, and is shown in Table 3. The equilibrium phase fractions and the carbon content in austenite (C_γ) at 840 °C, calculated using ThermoCalc, and the martensite-start temperatures (M_s) for these regions, calculated from Andrews equation [46], are also shown in Table 3.

The equilibrium data in Table 3 show a higher fraction of cementite and a lower C_γ for the solute-rich region in comparison to the solute-lean region. The corresponding M_s temperatures for the solute-rich and solute-lean regions are 125 °C and 120 °C, respectively. The expected volume fractions of martensite present in these regions at room temperature (25 °C) can be quantified using the Koistinen and Marburger (KM) model as [47]:

$$f^{\alpha'} = 1 - \exp[-\alpha_m(M_s - T)] \quad (1)$$

where $f^{\alpha'}$ is the volume fraction of martensite present at the temperature T (25 °C), M_s is the theoretical martensite-start temperature, and α_m is the rate parameter, taken as 0.011 $°C^{-1}$ [48]. From Eq. (1), the martensite fractions at room temperature in the solute-rich and solute-lean regions are 67% and 65%, respectively. The corresponding austenite fractions in the solute-rich and solute-lean regions, taking into account the cementite fractions from Table 3, are 31% and 33%, respectively. These theoretical phase fraction calculations show that the compositional differences in the chemical segregation bands are not strong enough to engender severe

Table 3 – Average chemical composition of the solute-rich and solute-lean regions, and the corresponding equilibrium phase fractions, the carbon content in austenite (C_γ) at 840 °C, and M_s temperatures.

	Elements (wt.%)						Phase (%)		C_γ (wt.%)	M_s (°C)
	C	Ni	Cr	Mn	Si	Mo	Austenite	Cementite		
Solute-rich region	0.85	3.5	1.6	0.6	0.4	0.25	98.0	2.0	0.74	125
Solute-lean region	0.85	3.1	1.4	0.5	0.3	0.18	98.6	1.4	0.78	120

phase heterogeneities after quenching, as the areas seen in Figs. 5 and 6.

Nonetheless, it is to be emphasized that both these equilibrium predictions (phase fractions and C_γ) are contrary to the experimental observations, which show that the solute-rich region has a lower cementite fraction, and consequently, a higher retained austenite fraction due to higher C_γ at 840 °C. The observed deviation of the theoretical and experimental fractions of phases indicates a significant impact of the starting microstructures on the thermodynamic and kinetic factors affecting austenite formation. Therefore, further analysis is required to explain the carbide-dense bands and differences in the austenite fractions in the chemical bands.

4.2.1. *Carbide-dense bands*

One of the heterogeneities observed in the hardened microstructure is the occurrence of carbide-dense bands, which are characterized by variations in the distribution, size, and density of carbides in the chemically segregated regions. Microstructures obtained after various time intervals (10 s, 300 s, 3600 s) at 840 °C are compared to the one obtained after 7200 s to investigate the origin for the carbide-dense bands. The SEM micrographs from the solute-lean (DER) and solute-rich (LER) regions are depicted in Fig. 11, which also indicates the corresponding heat treatments. Note that DER and LER are not separated by visually distinct boundaries. However, differentiation between the two regions can be made based on the significant etching contrast observed. Indentations were made, based on the optical microscopy contrast, as reference points to trace and capture the locations of interest using SEM.

The microstructural constituents in Fig. 11 are martensite, retained austenite, and cementite. A distinction between martensite and austenite is difficult to make from these micrographs. However, the cementite distribution is readily apparent. Due to the high cooling rate (50 °C/s), cementite is not expected to form as an austenite decomposition product during quenching. Therefore, the cementite in these microstructures is concluded to be a product of the microstructural changes occurring during the heating or the holding stage at 840 °C. Fig. 11 (a, e) show that cementite is present from the very beginning of the isothermal holding stage in both regions. Subsequent austenite formation depends on the dissolution kinetics of cementite [49,50], which is separately evaluated for each of the two regions.

4.2.1.1. *Solute-lean region (DER)*. The morphology and distribution of cementite in the solute-lean region after 10 s, 300 s, 3600 s, and 7200 s are shown in Fig. 11(a–d). After 10 s (Fig. 11(a)), disintegrated traces of the initial cementite morphology (elongated) are observed, together with globular cementite. The cementite distribution is homogeneous with an area fraction of 4.20 ± 0.03%, quantified using image analysis with ImageJ software. Within 300 s at 840 °C, around 1% of cementite has dissolved, and the elongated morphology of cementite is no longer visible. Instead, the microstructure has a high density of fine globular carbides (Fig. 11(b)). The dissolution kinetics of cementite becomes sluggish beyond 300 s. This is derived from the calculation of its area fraction, which is ≈ 3.10 ± 0.03% after 3600 s (Fig. 11(c)) and 3.00 ± 0.03% after 7200 s (Fig. 11(d)).

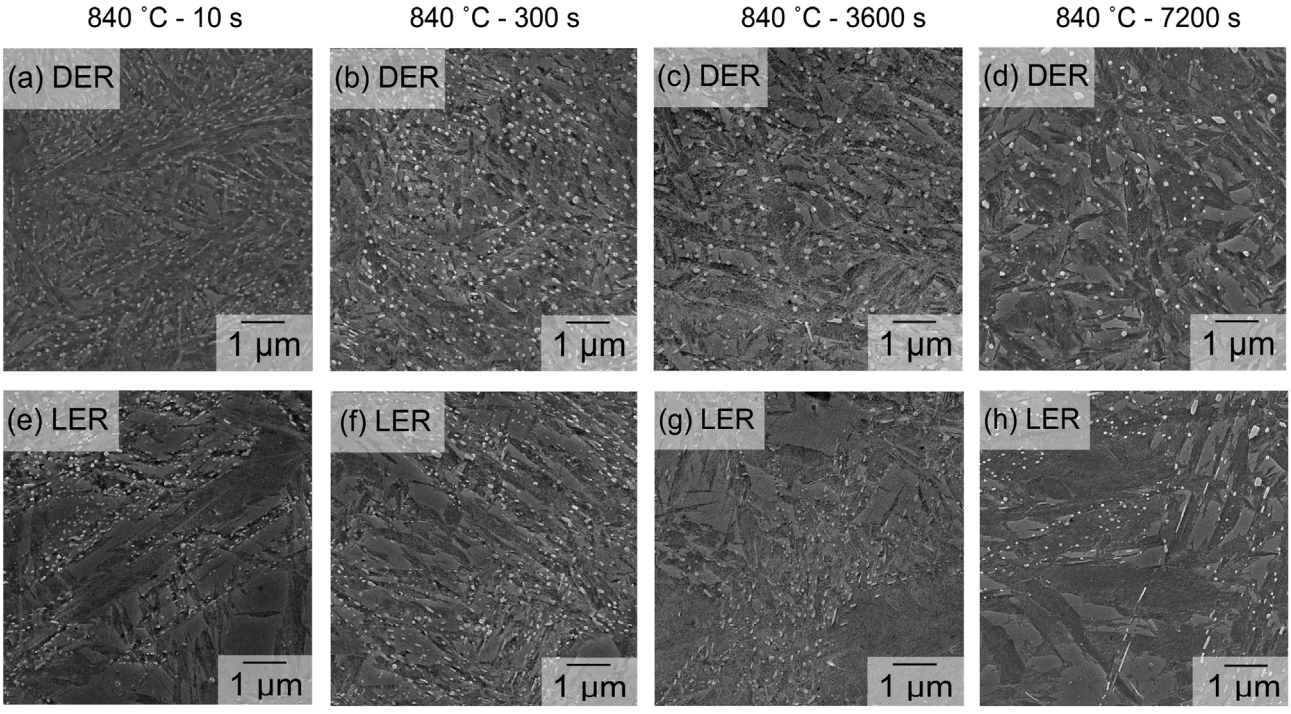

Fig. 11 – SEM micrographs (a–d) solute-lean regions (DER) and (e–h) solute-rich (LER) after the corresponding holding time at the hardening temperature (840 °C).

4.2.1.2. *Solute-rich region (LER)*. The morphology and distribution of cementite in the solute-rich region after 10 s, 300 s, 3600 s, and 7200 s are shown in Fig. 11(e–h). Despite its absence in the initial microstructure of the solute-rich regions, Fig. 11(e) shows that cementite is present (2.90 ± 0.03%) from a very early stage of isothermal holding. The cementite particles seen in Fig. 11(e) likely formed during the heating stage due to the supersaturated state of the martensite. The distribution of cementite is seen to be very inhomogeneous and has a preferential growth along the martensite block/lath boundaries. The area fractions of cementite after 300, 3600, and 7200 s are 2.5, 2.4, and 2.2%, respectively. The error for these measurements is 0.03%, indicating that the values are precise and reliable within this range.

While cementite distribution is homogeneous in the solute-lean region of the hardened microstructure, its distribution in the solute-rich area is mainly in the vicinity of the prior martensite, from which cementite precipitates during heating. Based on microstructural observations, a reason for the carbide-dense bands is proposed. The initial microstructure in the solute-lean region is bainitic, in which the cementite constituents are homogeneously distributed (see Fig. 1(b)). As the temperature reaches A_{c1}, the bainitic ferrite begins to transform into austenite, and this transformation is complete at A_{c3}. However, cementite is stable in the entire temperature window of continuous heating. Consequently, a homogeneous distribution of cementite is observed at the onset of isothermal holding at 840 °C. Although around 1% cementite dissolves in the first few minutes of isothermal holding, the subsequent dissolution of cementite is significantly impeded, resulting in the preservation of its original spatial arrangement, which remains almost unchanged even after 2 h.

On the other hand, the initial microstructure in the solute-rich region is martensite mixed with austenite. Both these phases are metastable at low temperatures and have a high driving force for transformation into ferrite and cementite, which can take place during heating. While cementite precipitates from the supersaturated martensite with the rise in temperature, the austenite formation is only partial, see Fig. 8. A significant fraction of austenite (20%) remains stable up to A_{c1}. This retained fraction of austenite grows without the need for nucleation at temperatures beyond A_{c1}. Therefore, cementite precipitation is inhibited in regions where austenite remained stable during heating. Consequently, at the onset and for the entire duration of isothermal holding, cementite is observed only in the vicinity of the prior martensite.

4.2.2. *Dissolution kinetics of cementite during isothermal holding*

The isothermal austenite formation at 840 °C in the investigated steel occurs in the presence of cementite, which involves the movement of γ/θ phase boundaries into the latter and diffusion of both interstitial and substitutional alloying elements. The partitioning of the alloying elements plays a role in the transformation kinetics of phases. In the current scenario, cementite dissolution during the initial stages of holding is characterized by rapid dissolution, followed by a subsequent slower dissolution. This experimental trend was validated by assessing the dissolution rate of cementite at 840 °C, plotted using DICTRA simulations as shown in Fig. 12.

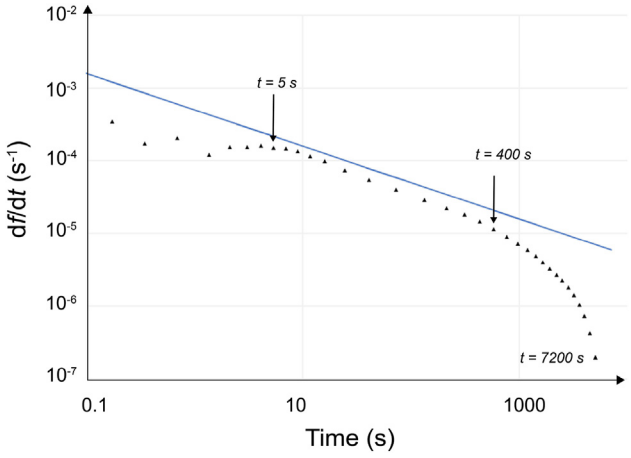

Fig. 12 – Transformation rate of cementite during isothermal holding at 840 °C calculated with DICTRA.

Fig. 12 shows the rate of dissolution of cementite. The initial data points in the simulation results were excluded due to potential numerical artifacts arising from the discretization and numerical methods employed in the simulations. The blue line represents a diffusion-controlled transformation, where the transformation rate is inversely proportional to the square root of time (*t*). It is observed that for time du-rations $t < 5$ s, a transition is occurring that deviates from pure diffusion-controlled behavior, exhibiting some variability around it. Possible reasons for the observed deviation from pure diffusion-controlled behavior could include initial transient behavior, numerical artifacts, or non-ideal simulation conditions. After $t \approx 5$ s, the slope is consistent with diffusion-controlled transformation, until $t \approx 400$ s, after which the transformation rate strongly decreases. This simulation result effectively captures the experimental trend related to the dissolution of cementite.

In steels containing Mn and Cr, the dissolution kinetics of cementite in austenite is influenced not only by carbon, but also by the partitioning and redistribution of Mn and Cr within both austenite and cementite. Therefore, the concentration profiles of C, Cr, and Mn at various time intervals are investigated to gain more insight into the observed experimental results from interrupted quench experiments. Fig. 13(a), (b), and (c) shows the concentration profiles of C, Cr, and Mn, respectively, in cementite and austenite at various time intervals; 0, 10, 300, 3600, and 7200 s. Given the rapid diffusion of carbon in austenite, the equilibrium composition of carbon at 840 °C (0.8 wt%) is used as the initial value for the simulation, while nominal composition values of 1.5 wt% for Cr and 0.55 wt% for Mn are inputted as the initial compositions of both phases. The θ/γ interface at $t = 0$ s is at 150 nm, indicated by the dotted vertical lines.

Fig. 13 (a) shows that the concentration profile of carbon becomes flat within a few seconds due to its fast diffusion, with

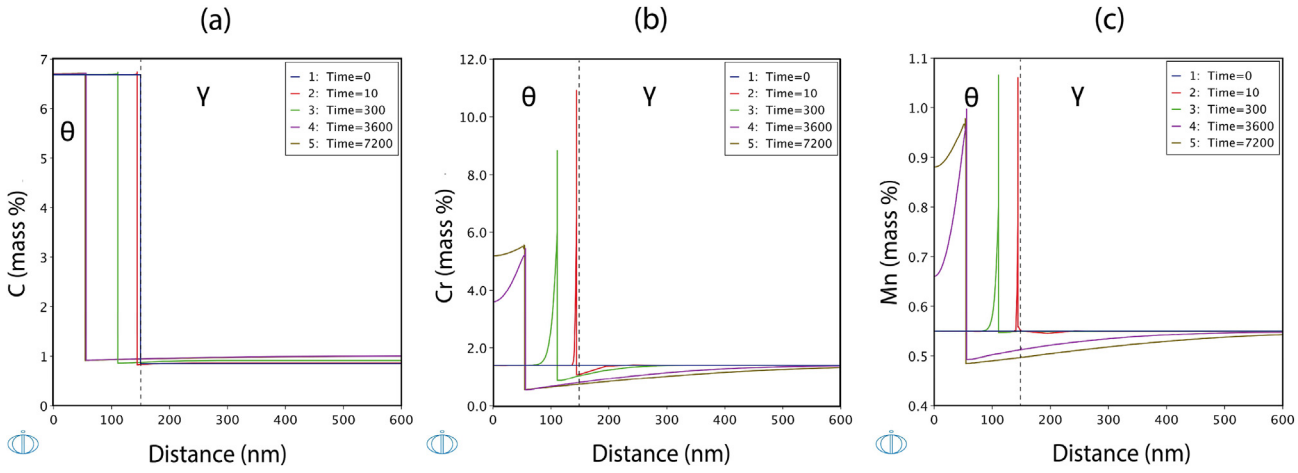

Fig. 13 – Concentration profiles as a function of holding time at 840 °C for (a) C, (b) Cr, and (c) Mn calculated using DICTRA. Note that the austenite domain extends to 3750 nm. Indicated times are in seconds.

the actual time likely being even shorter than the 10 s of the shown simulation result. On the other hand, the concentration profiles of Cr and Mn, depicted in Fig. 13(b and c), exhibit significantly inhomogeneous distributions in cementite and austenite even after 7200 s. During the early stages of isothermal holding at $t = 10$ s and $t = 300$ s, both Cr and Mn concentration profiles exhibit a spike at the interface between cementite and austenite. However, the nominal concentration values of Cr and Mn in cementite, located far from the growing austenite matrix, remain unchanged. The observed spike in Cr and Mn concentration profiles at the θ/γ interface at $t = 10$ s and $t = 300$ s indicates the rapid dissolution of cementite, driven by carbon diffusion, and limited diffusion of Cr and Mn across the interface. This limited diffusion leads to insufficient time for complete redistribution and equilibration of Cr and Mn, resulting in the concentration spike at the interface. With the progress in holding, at $t = 3600$ s, cementite is increasingly enriched with Cr and Mn. This enrichment results from the partitioning of Cr and Mn into cementite from the newly formed austenite, which results in gradually reducing the concentration gradients over time. Although the concentrations of Mn and Cr in cementite are not homogeneous even after 7200 s, cementite remains stable as can be seen from the negligible growth of θ/γ interface into cementite (see Fig. 13(b and c) for $t = 3600$ s and 7200 s). Therefore, it is reasonable to conclude that the sluggish dissolution of cementite after 400 s is primarily caused by its enrichment with Mn and Cr. This conclusion is in agreement with several previous studies [51–54]. It is to be emphasized that the concentration spike for Mn at the interface at $t = 10$ s starts at a value which is slightly higher than equilibrium (1.01%). The exact reason for this behavior is unknown. However, it is clear that Mn, like Cr, gradually partitions into cementite over time, thereby reducing the concentration gradients and contributing to the sluggish dissolution of cementite.

4.2.3. *Heterogeneous distribution of retained austenite*

Cementite formation during austenitization reduces the carbon concentration in austenite, which decreases its resistance to martensite formation. Consequently, the fractions of these phases in the quenched microstructure are interdependent such that a higher fraction of cementite will result in a lower retained austenite fraction. The equilibrium fractions of cementite in the solute-rich and solute-lean regions of the hardened microstructure are 2.2% and 3.0%, respectively, as discussed in section 4.2.1. The carbon content in austenite (C_γ) at the onset of quenching in the two regions can be calculated from the carbon-mass balance given by

$$C_\gamma = \frac{1}{V_\gamma[\bar{x} - C_\theta V_\theta]} \tag{2}$$

where $\bar{x}$ is the carbon content in the alloy (0.85 wt%), C_θ is the carbon content in cementite (6.67 wt%), V_γ is the volume fraction of austenite, and V_θ is the volume fraction of cementite.

From Eq. (2), C_γ for the solute-rich and solute-lean regions are 0.73 and 0.68 wt%, respectively. These values correspond to M_s temperatures of 130 °C in the solute-rich region and 160 °C in the solute-lean area, calculated from Andrews equation [46]. The corresponding martensite fractions calculated using Eq. (1) are 68% for the solute-rich region and 77% in the solute-lean region. Taking into account the cementite fractions in these regions: 2.2% in solute-rich and 3.0% in the solute-lean regions, the retained austenite fractions are 29% and 20%, respectively. These values are in close accordance with experimental observations (30% in solute-rich and 24% in solute-lean regions) and explain the heterogeneity for the phase fractions in the chemical bands.

5. Conclusions

Austenite formation from a microstructure consisting of bainite (solute-lean region) and martensite/austenite (solute-rich region) bands in high-C steel containing Ni and Cr was investigated by in situ XRD analysis, microstructural observations, and DICTRA simulations. The following conclusions are drawn from this study.

- Differences in the austenite formation mechanisms can result in a bimodal austenite grain size distribution. Refinement of the prior austenite grains occurs during austenite formation from bainite, which proceeds by the typical nucleation and growth process. However, austenite formation from a mixture of martensite and retained austenite does not lead to grain refinement. The inhibition of grain refinement is assumed to be a result of a memory effect resulting from the growth, impingement, and coalescence of existing austenite during heating, which reconstitutes the prior austenitic structure without the need for fresh nucleation.
- Carbide-dense bands appear in a hardened microstructure characterized by variations in the size, density, and distribution of carbides. The formation of such bands depends not only on the dissolution kinetics of carbides during austenitization but also on its initial microstructure-dependent distribution in the austenite matrix at the onset of holding.
- The dissolution kinetics of cementite predicted using DICTRA simulations during the isothermal austenitization process shows an initially rapid dissolution, which however becomes sluggish with the enrichment of Cr and Mn in cementite.
- The presence of cementite during isothermal austenite formation affects the carbon content in austenite. A higher fraction of cementite is observed in the solute-lean region compared to the solute-rich region. From carbon mass balance calculations, it is shown that a very small difference of 0.05 wt% C for the carbon content in austenite at the onset of quenching leads to a 30 °C difference in M_s. This difference is significant to engender inhomogeneous distribution of retained austenite in the hardened microstructure.

Declaration of competing interest

The authors declare the following financial interests/personal relationships which may be considered as potential competing interests:

J. Abraham Mathews reports financial support was provided by SKF Research and Technology Development. J. Abraham Mathews reports financial support was provided by Siemens Gamesa Renewable Energy (Denmark). J. Abraham Mathews reports financial support was provided by Top consortium for Knowledge and Innovation (TKI).

Acknowledgments

The authors gratefully acknowledge the grant provided by Siemens Gamesa Renewable Energy (Denmark), SKF Research and Technology Development (The Netherlands), and the Dutch government through Top consortium for Knowledge and Innovation (TKI). The industrial partners of this project, Siemens Gamesa Renewable Energy (Denmark) and SKF Research and Technology Development (The Netherlands) are also acknowledged for providing the materials. The authors would like to thank Mr. Ruud Hendrikx and Drs. Richard Huizenga at the Department Materials Science and Engineering of the Delft University of Technology for the X-ray analysis, and Ing. C. Kwakernaak for performing EPMA measurements. The authors extend. Their gratitude to Dr. Stefan Melzer (Tata Steel, IJmuiden, The Netherlands) for the in situ XRD experiment and Jiayu Li (Ghent University) for EBSD measurements.

REFERENCES

[1] Karthikeyan T, Dash MK, Mythili R, Selvi SP, Moitra A, Saroja S, et al. Effect of prior-austenite grain refinement on microstructure, mechanical properties and thermal embrittlement of 9Cr-1Mo-0.1C steel. J Nucl Mater 2017;494:260–77.
[2] Karthikeyan T, Paul VT, Saroja S, Moitra A, Sasikala G, Vijayalakshmi M. Grain refinement to improve impact toughness in 9Cr–1Mo steel through a double austenitization treatment. J Nucl Mater 2011;419:256–62.
[3] Sanij MK, Banadkouki SG, Mashreghi A, Moshrefifar M. The effect of single and double quenching and tempering heat treatments on the microstructure and mechanical properties of aisi 4140 steel. Mater Des 2012;42:339–46.
[4] Morito S, Yoshida H, Maki T, Huang X. Effect of block size on the strength of lath martensite in low carbon steels. Mater Sci Eng, A 2006;438:237–40.
[5] Hidalgo J, Santofimia MJ. Effect of prior austenite grain size refinement by thermal cycling on the microstructural features of as-quenched lath martensite. Metall Mater Trans 2016;47:5288–301.
[6] Matsuda S, Inoue T, Mihura H, Okamura Y. Toughness and effective grain size in heat-treated low-alloy high strength steels. Transactions of the Iron and Steel Institute of Japan 1972;12:325–33.
[7] Zhen F, Zhang K, Guo Z-l, Qu J-b. Effect of martensite fine structure on mechanical properties of an 1100 MPa grade ultra-high strength steel. J Iron Steel Res Int 2015;22:645–51.
[8] Li S, Zhu G, Kang Y. Effect of substructure on mechanical properties and fracture behavior of lath martensite in 0.1 C-1.1 Si-1.7 Mn steel. J Alloys Compd 2016;675:104–15.
[9] Hamada A, Karjalainen L, Surya PV, Misra R. Fatigue behavior of ultrafine-grained and coarse-grained Cr-Ni austenitic stainless steels. Mater Sci Eng, A 2011;528:3890–6.
[10] Di Schino A, Kenny J. Grain size dependence of the fatigue behaviour of a ultrafine-grained AISI 304 stainless steel. Mater Lett 2003;57:3182–5.
[11] Liu H, Fu P, Liu H, Sun C, Du N, Li D. Simultaneously enhancing strength and toughness of medium-carbon martensitic steel via nano precipitates and fine-grained structure. Mater Sci Eng, A 2022;842:143030.
[12] Li X, Ma X, Subramanian S, Shang C, Misra R. Influence of prior austenite grain size on martensite–austenite constituent and toughness in the heat affected zone of 700 MPa high strength linepipe steel. Mater Sci Eng, A 2014;616:141–7.
[13] Oliveira FLG, Andrade MS, Cota AB. Kinetics of austenite formation during continuous heating in a low carbon steel. Mater Char 2007;58:256–61.
[14] Mohanty R, Girina O, Fonstein N. Effect of heating rate on the austenite formation in low- carbon high-strength steels annealed in the intercritical region. Metall Mater Trans 2011;42:3680.

[15] Esin VA, Denand B, Le Bihan Q, Dehmas M, Teixeira J, Geandier G, et al. In situ synchrotron X-ray diffraction and dilatometric study of austenite formation in a multi-component steel: influence of initial microstructure and heating rate. Acta Mater 2014;80:118–31.
[16] Yang J, Bhadeshia H. Continuous heating transformation of bainite to austenite. Mater Sci Eng, A 1991;131:99–113.
[17] Savran V, Leeuwen Y, Hanlon D, Kwakernaak C, Sloof W, Sietsma J. Microstructural features of austenite formation in C35 and C45 alloys. Metall Mater Trans 2007;38:946–55.
[18] Schmidt E, Wang Y, Sridhar S. A study of nonisothermal austenite formation and decomposi- tion in Fe-C-Mn alloys. Metall Mater Trans 2006;37:1799.
[19] Speich G, Demarest V, Miller R. Formation of austenite during intercritical annealing of dual- phase steels. Metall Mater Trans 1981;12:1419–28.
[20] Savran V, Offerman S, Sietsma J. Austenite nucleation and growth observed on the level of in- dividual grains by three-dimensional x-ray diffraction microscopy. Metall Mater Trans 2010;41:583–91.
[21] Saito R, Nakada N, Yabu S, Hayashi K. Effects of initial structure and reversion temperature on austenite nucleation site in pearlite and ferrite–pearlite. Metall Mater Trans 2018;49:6001–9.
[22] Bhadeshia HKDH, Christian J. Bainite in steels. Metall Trans A 1990;21:767–97.
[23] Kimmins S, Gooch D. Austenite memory effect in 1Cr–1Mo–0.75V (Ti, B) steel. Met Sci 1983;17:519–32.
[24] Hara T, Maruyama N, Shinohara Y, Asahi H, Shigesato G, Sugiyama M, et al. Abnormal α to γ transformation behavior of steels with a martensite and bainite microstructure at a slow reheating rate. ISIJ Int 2009;49:1792–800.
[25] Shinozaki T, Tomota Y, Fukino T, Suzuki T. Microstructure evolution during reverse trans- formation of austenite from tempered martensite in low alloy steel. ISIJ Int 2017;57:533–9.
[26] Homma R. Studies on austenite grain of 3.5% Ni-Cr-Mo-V steel. Transactions of the Iron and Steel Institute of Japan 1974;14:434–43.
[27] Liu L, Yang Z-G, Zhang C. Effect of retained austenite on austenite memory of a 13% Cr–5% Ni martensitic steel. J Alloys Compd 2013;577:S654–60.
[28] Shirazi H, Miyamoto G, Nedjad SH, Chiba T, Ahmadabadi MN, Furuhara T. Microstruc- ture evolution during austenite reversion in fe-ni martensitic alloys. Acta Mater 2018;144:269–80.
[29] Zhang X, Miyamoto G, Toji Y, Nambu S, Koseki T, Furuhara T. Orientation of austenite reverted from martensite in Fe-2Mn-1.5Si-0.3C alloy. Acta Mater 2018;144:601–12.
[30] Bhadeshia H. Steels for bearings. Prog Mater Sci 2012;57:268–435.
[31] Adishesha P. Effect of steel making and processing parameters on carbide banding in com- mercially produced ASTM A-295 52100 bearing steel. ASTM (Am Soc Test Mater) Spec Tech Publ 2002;1419:27–46.
[32] Verhoeven JD. A review of microsegregation induced banding phenomena in steels. J Mater Eng Perform 2000;9:286–96.
[33] Hellner L, Norrman T. Banding in alloy steels. Jernkontorets Ann 1968;152:269–86.
[34] Krishna SC, Tharian KT, Chakravarthi K, Jha AK, Pant B. Heat treatment and thermo- mechanical treatment to modify carbide banding in aisi 440C steel: a case study. Metallography, Microstructure, and Analysis 2016;5:108–15.
[35] Manwatkar SK, Bahrudheen A, Tiwari SB, Narayana Murty S, Ramesh Narayanan P. Failure analysis of aisi 440C steel ball screws used in the actuator system of a satellite launch vehicle. J Fail Anal Prev 2017;17:505–12.
[36] Walker P, Kerrigan A, Green M, Cardinal N, Connell J, Rivera-Dáıaz-del Castillo P. Mod- elling of micro-segregation in a 1C-1.5Cr type bearing steel. In: Bearing steel technologies: 10th volume, advances in steel technologies for rolling bearings. ASTM International; 2015.
[37] Mathews JA, Sietsma J, Petrov R, Santofimia M. Influence of chemical segregation on bainitic microstructures in a carburized bearing steel. Mater Des 2022:111232.
[38] Yang J, Bhadeshia H. Reaustenitization experiments on some high-strength steel weld deposits. Mater Sci Eng, A 1989;118:155–70.
[39] Middleton C, Form G. Direct observation of an austenite memory effect in low-alloy steels. Met Sci 1975;9:521–8.
[40] Zhang L, Guo DC. A general etchant for revealing prior-austenite grain boundaries in steels. Mater Char 1993;30:299–302.
[41] Zhang X, Miyamoto G, Toji Y, Zhang Y, Furuhara T. Role of cementite and retained austenite on austenite reversion from martensite and bainite in fe-2Mn-1.5 Si-0.3 C alloy. Acta Mater 2021;209:116772.
[42] Wu Y, Wang L, Sun W, Styles M, Studer A, Breáchet Y, et al. Austen- ite formation kinetics from multicomponent cementite-ferrite aggregates. Acta Mater 2020;196:470–87.
[43] Wu H-Y, Su Y-HF, Lin G-R, Kuo J-C. Effect of cooling rate on carbide banding in high- chromium bearing steel after spheroidization. Metall Mater Trans 2020;51:4471–82.
[44] Majka TF, Matlock DK, Krauss G. Development of microstructural banding in low-alloy steel with simulated Mn segregation. Metall Mater Trans 2002;33:1627–37.
[45] Wu W, Hwu L, Lin D, Lee J. The relationship between alloying elements and retained austenite in martensitic stainless steel welds. Scripta Mater 2000;42:1071–6.
[46] Andrews K. Empirical formulae for the calculation of some transformation temperatures. J. Iron Steel Inst. 1965:721–7.
[47] Koistinen DP, Marburger RE. A general equation prescribing the extent of the austenite- martensite transformation in pure iron-carbon alloys and plain carbon steels. Acta Metall 1959;7:59–60.
[48] Van Bohemen SMC, Sietsma J. Modeling of isothermal bainite formation based on the nucle- ation kinetics. Int J Mater Res 2008;99:739–47.
[49] Liu Z-K, Hö glund L, Jönsson B, ågren J. An experimental and theoretical study of cementite dissolution in an Fe-Cr-C alloy. Metall Trans A 1991;22:1745–52.
[50] Chae J-Y, Jang J-H, Zhang G, Kim K-H, Lee JS, Bhadeshia H, et al. Dilatometric analysis of cementite dissolution in hypereutectoid steels containing cr. Scripta Mater 2011;65:245–8.
[51] Mueller J, Hu X, Sun X, Ren Y, Choi K, Barker E, et al. Austenite formation and cementite dissolution during intercritical annealing of a medium-manganese steel from a martensitic condition. Mater Des 2021;203:109598.
[52] Estay S, Chengji L, Purdy G. Carbide dissolution and austenite growth in the intercritical annealing of fe–c–mn dual phase steels. Can Metall Q 1984;23:121–30.
[53] Zhao L, Vermolen F, Sietsma J, Wauthier A. Cementite dissolution at 860 °C in an Fe-Cr-C steel. Metall Mater Trans 2006;37:1841–50.
[54] Zhang G-H, Chae J-Y, Kim K-H, Suh DW. Effects of Mn, Si and Cr addition on the dissolution and coarsening of pearlitic cementite during intercritical austenitization in Fe-1mass% C alloy. Mater Char 2013;81:56–67.